

## The metallicity and distance of Leo A from blue supergiants

MIGUEL A. URBANEJA,<sup>1</sup> FABIO BRESOLIN,<sup>2</sup> AND ROLF-PETER KUDRITZKI<sup>2,3</sup>

<sup>1</sup>*Universität Innsbruck, Institut für Astro- und Teilchenphysik  
Technikerstr. 25/8, 6020 Innsbruck, Austria*

<sup>2</sup>*Institute for Astronomy, University of Hawaii  
2680 Woodlawn Drive*

*Honolulu, HI 96822, USA*

<sup>3</sup>*University Observatory Munich, Scheinerstr. 1, D-81679 Munich, Germany*

### ABSTRACT

We have obtained high-quality spectra of blue supergiant candidates in the dwarf irregular galaxy Leo A with the Low Resolution Imaging Spectrometer at the Keck I telescope. From the quantitative analysis of seven B8-A0 stars we derive a mean metallicity  $[Z] = -1.35 \pm 0.08$ , in excellent agreement with the gas-phase chemical abundance. From the stellar parameters and the flux-weighted–luminosity relation (FGLR) we derive a spectroscopic distance modulus  $m - M = 24.77 \pm 0.11$  mag, significantly larger ( $\sim 0.4$  mag) than the value indicated by RR Lyrae and other stellar indicators. We explain the bulk of this discrepancy with blue loop stellar evolution at very low metallicity and show that the combination of metallicity effects and blue loop evolution amounts, in the case of Leo A, to a  $\sim 0.35$  mag offset of the FGLR to fainter bolometric luminosities. We identify one outlier of low bolometric magnitude as a post-AGB star. Its metallicity is consistent with that of the young population, confirming the slow chemical enrichment of Leo A.

*Keywords:* Galaxy abundances(574) — Galaxy stellar content(621) — Stellar abundances(1577)

### 1. INTRODUCTION

The dwarf irregular galaxy Leo A (DDO 69, UGC 5364), at a distance of 0.76 Mpc (Nagarajan et al. 2022), is among the gas-rich systems with the lowest gas-phase metallicity known in the nearby universe,  $12 + \log(\text{O}/\text{H}) \simeq 7.4^1$  (Ruiz-Escobedo et al. 2018). Its delayed, low-level star formation activity (Cole et al. 2007) has been related to its isolation (Cole et al. 2014; Gallart et al. 2015), as Leo A assembled in a low-density environment near the edge of the Local Group, several hundreds of kpc from both the Milky Way and M31 (McConnachie 2012). Leo A offers the opportunity for a rare glimpse into the properties and chemistry of young stars

in unevolved star-forming environments attainable from high-quality spectra.

The first spectroscopic investigation of individual stars in Leo A was carried out by Brown et al. (2007), who derived the stellar velocity dispersion of the galaxy from spectra of 10 B supergiants (two of these were included in their previous search for hypervelocity stars: Brown et al. 2006) and two H II regions. The spectroscopic analysis of the older population of red giants has been presented by Kirby et al. (2017), enlarging the sample of Kirby et al. (2013). They derived a mean  $[\text{Fe}/\text{H}] = -1.67$ , only slightly below the gas-phase metallicity, suggesting a slow chemical enrichment in Leo A, in agreement with the flat age-metallicity relation derived from Hubble Space Telescope (HST) photometry by Cole et al. (2007). More recently, Gull et al. (2022) derived stellar parameters for a sample of massive stars (late O/early B main-sequence objects) in Leo A from both HST photometry and ground-based spectroscopy.

With this paper we contribute to the spectroscopic investigation of individual stars in Leo A and the present-day metal content of this galaxy by focusing on blue

Corresponding author: Miguel.Urbaneja-Perez  
Miguel.Urbaneja-Perez@uibk.ac.at, bresolin@ifa.hawaii.edu,  
kud@ifa.hawaii.edu

<sup>1</sup> This value corresponds to  $[\text{O}/\text{H}] \simeq -1.3$  (5% of the oxygen abundance of the Sun) with the solar oxygen abundance of Asplund et al. (2009) adopted here.

supergiants (BSGs), i.e. evolved massive stars. We use a comprehensive grid of model atmosphere spectra based on detailed and extensive non-LTE calculations to determine stellar temperatures, gravities, luminosities and metallicities together with interstellar extinction. As we have shown in the work by our team over the last two decades (see Kudritzki et al. 2008, 2012, 2016; Urbaneja et al. 2008, 2017; Bresolin et al. 2016, 2022, and further references therein) by studying more than a dozen nearby galaxies, this method of quantitative spectral analysis provides accurate information about galaxy metallicity and metallicity gradients as well as distances. It provides an excellent basis to understand galaxy evolution, for instance, by investigating the observed mass-metallicity relationship of galaxies (Kudritzki et al. 2021). In this regard Leo A, as a potentially extremely metal-poor galaxy, is especially interesting.

The challenge of a BSG study in Leo A is the relative faintness of the targets ( $V \sim 19-21$ ), together with their low metallicity and the correspondingly weak metal lines. This challenge is met with high-quality spectra of high signal-to-noise ratio (up to  $\sim 200$ ) obtained in a long sequence of exposures with the LRIS spectrograph at the Keck telescope. Our approach to deriving stellar parameters and metallicities is the same we adopted in previous work on galaxies of higher chemical abundances (for a recent example, see Bresolin et al. 2022 and references therein). In Sect. 2 we present observations, data reduction and spectral classification of the targets. The quantitative analysis of seven late-B/early-A stars is described in Sect. 3. We then use the parameters for these objects to briefly discuss the location of Leo A in the stellar mass-metallicity relation of star-forming galaxies (Sect. 4) and the spectroscopic distance we derive (Sect. 5). Considerations on a post-AGB star that we have serendipitously discovered in Leo A are presented in Sect. 6. We summarize our results in Sect. 7.

## 2. OBSERVATIONS AND DATA REDUCTION

### 2.1. Target selection

We selected blue supergiant candidates for the spectroscopic observations from stellar photometry of archival HST/ACS imaging (Program: 10590; PI: Cole) in the F475W and F814W filters that we carried out using DOLPHOT (Dolphin 2000, 2016). Additional targets were selected outside the ACS field of view from published photometry of bright stars in Leo A from the Sloan Digital Sky Survey (SDSS, Adelman-McCarthy et al. 2007). Our final list for the multi-object spectroscopy consisted of 12 stars, selected to be brighter

than  $B = 22.0$  and bluer than  $B - I = 0.1$ . These criteria serve the purpose of isolating early-type supergiant candidates of sufficient brightness for our quantitative analysis, affected by only a small amount of reddening.

A summary of positions,  $V$  magnitudes and  $B - V$ ,  $V - I$  color indices of the 12 targets is presented in Table 1. The photometric information is extracted from the work of Stonkutė et al. (2014), which we prefer to adopt here over our original photometry because of the additional color information and the larger spatial coverage. Figure 1 displays the location of these objects.

### 2.2. Spectroscopy

We collected the spectra of our BSG candidates with the Low Resolution Imaging Spectrometer (LRIS, Oke et al. 1995) at the Keck I telescope, during the course of six nights, distributed over three distinct observing campaigns in 2012, 2013 and 2015. Leo A was observed at the start of each night, when our main target, NGC 4258, was too low above the horizon to be observed (Kudritzki et al., in preparation).

The multi-object spectroscopy was obtained employing a single slit mask. With the selected 600/4000 grism and 1"2 slit width our data cover the approximate wavelength range 3300–5600 Å with a FWHM spectral resolution of about 5 Å. Individual exposure times varied between 1500s and 2700s, for a total integration time of 5.9 h.

The data reduction was carried out with IRAF<sup>2</sup>, and included the usual steps of bias subtraction, flat field correction and wavelength calibration. The spectral extractions for individual exposures were registered with the aid of sky lines and later combined. Finally, we rectified the combined spectra using low-order polynomials, and applied a radial velocity correction based on stellar lines in order to work with spectra in the rest frame. After completion of these steps, the average signal-to-noise ratio of the coadded spectra ranges between 40 and 220 (median: 140). We display in Figure 2 the final spectra of the 12 targets in the 3800–5050 Å interval.

### 2.3. Spectral classification

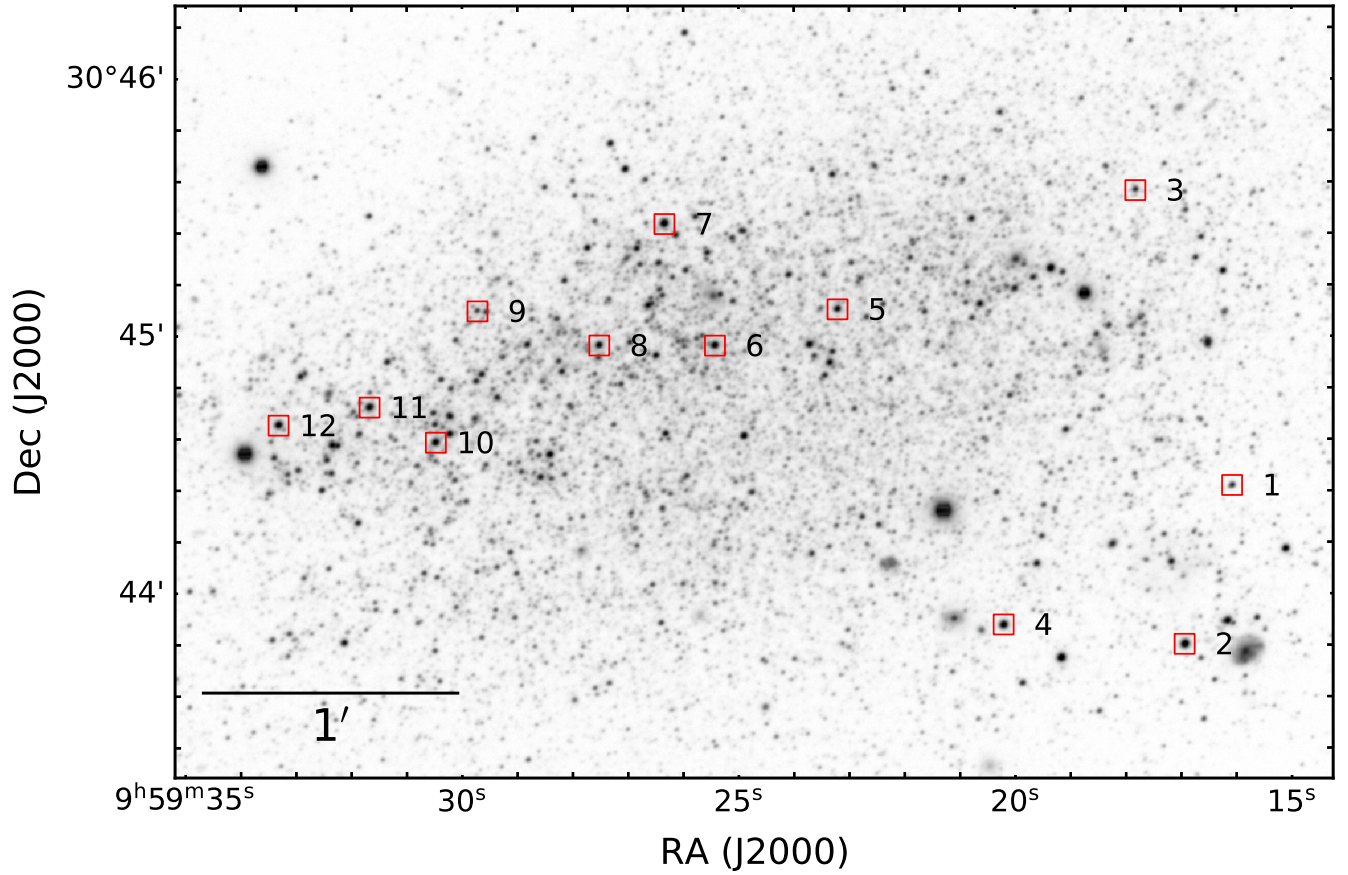
The classification of early-type stars of low metallicity requires an adjustment to the MK criteria since these are established from Galactic standards. Attempts to devise a stellar classification system for LMC and SMC stars were introduced by Fitzpatrick (1991)

<sup>2</sup> IRAF was distributed by the National Optical Astronomy Observatory, which was managed by the Association of Universities for Research in Astronomy (AURA) under a cooperative agreement with the National Science Foundation.

**Table 1.** Properties of the spectroscopic targets.

| ID   | R.A.<br>(J2000.0) | Decl.<br>(J2000.0) | $V$<br>(mag) | $B - V$<br>(mag) | $V - I$<br>(mag) | Spectral<br>type |
|------|-------------------|--------------------|--------------|------------------|------------------|------------------|
| (1)  | (2)               | (3)                | (4)          | (5)              | (6)              | (7)              |
| 01   | 09 59 16.08       | 30 44 25.2         | 21.36        | -0.19            | -0.14            | (B5 II)          |
| 02   | 09 59 16.94       | 30 43 48.2         | 19.27        | -0.11            | 0.00             | B2 Iab           |
| 03 * | 09 59 17.82       | 30 45 34.0         | 21.15        | -0.03            | 0.05             | (A0 II)          |
| 04 * | 09 59 20.21       | 30 43 52.8         | 19.65        | -0.07            | -0.01            | B8 Ib            |
| 05 * | 09 59 23.21       | 30 45 06.3         | 20.27        | -0.07            | 0.00             | B8 Ib            |
| 06 * | 09 59 25.43       | 30 44 57.8         | 19.85        | -0.06            | -0.04            | B8 Ib            |
| 07 * | 09 59 26.34       | 30 45 26.2         | 19.33        | -0.06            | -0.02            | B8 Ib            |
| 08   | 09 59 27.52       | 30 44 57.9         | 20.31        | -0.24            | -0.25            | O9 V             |
| 09   | 09 59 29.72       | 30 45 05.8         | 21.49        | 0.04             | 0.09             | (A0 III)         |
| 10 * | 09 59 30.48       | 30 44 35.2         | 19.70        | 0.08             | 0.20             | A0 II            |
| 11 * | 09 59 31.67       | 30 44 43.4         | 19.97        | -0.20            | 0.03             | B8 Ib            |
| 12   | 09 59 33.32       | 30 44 39.2         | 19.80        | -0.13            | 0.03             | O7/O8 V          |

NOTE—Stars identified with the asterisk in column (1) are those analyzed in Sect. 3. Photometric information taken from [Stonkutė et al. \(2014\)](#). Spectral types within parentheses in column (7) are considered uncertain.


**Figure 1.** Identification of the spectroscopic targets in a Subaru  $B$ -band image of Leo A taken from [Stonkutė et al. \(2014\)](#).

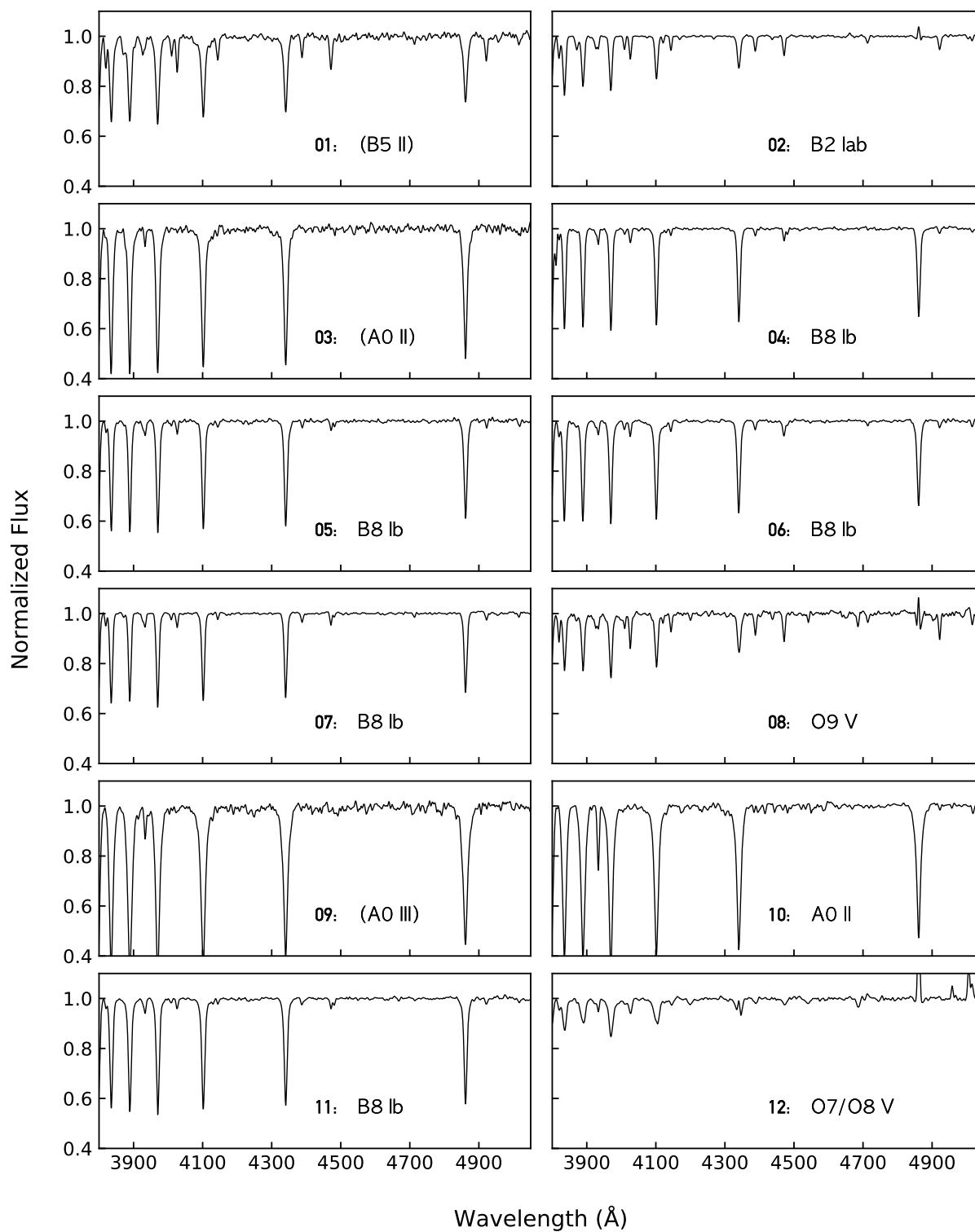


**Figure 2.** Compilation of the spectra of the 12 targets observed.

and Lennon (1997), respectively. In our previous blue supergiant work in low-metallicity galactic environments (WLM -  $[O/H] = -0.86$ : Bresolin et al. 2006; NGC 3109 -  $[O/H] = -0.93$ : Evans et al. 2007; IC 1613 -  $[O/H] = -0.79$ : Bresolin et al. 2007) we have followed the suggestion by Lennon (1997) to base the classification of B-type stars on trends of metal line strengths. For A-type stars, we followed instead Evans & Howarth (2003) and Evans et al. (2004), while for O stars we used the work by Walborn (1971), Walborn & Fitzpatrick (1990) and Walborn et al. (2000). In the case of Leo A, where stars have even weaker metal lines, we have relied on the same criteria, including the Ca II K/(Ca II H + He) line ratio (A stars), the relative strengths of the He I, Si II, Si III and Mg II lines (B stars), and the relative strengths of the He II and He I lines (O stars).

The equivalent width of the  $H\gamma$  line,  $W_\gamma$ , was used as a guidance to determine the luminosity classes, following Balona & Crampton (1974) and Azzopardi (1987). Our results show that, in addition to two late-O dwarfs, our sample includes several class II/III B- and A-type objects. The brightest stars are of class Iab/Ib, and range in absolute magnitude between  $M_V \simeq -5.1$  to  $M_V \simeq -4.1$ , significantly fainter than stars we have analyzed in more massive and more actively star-forming galaxies, where  $M_V$  can be as bright as  $-8$  to  $-9$ .

We note that six of our 12 targets were included in the velocity dispersion study of Brown et al. (2007). Using spectra of inferior quality compared to our Keck data, Brown et al. (2007) concluded that 10 of those were likely B supergiants of class I or II, whilst the remaining two objects were H II regions. Of the six objects in common with the aforementioned work, we confirm that four of those that Brown et al. identified as B supergiants are indeed supergiant stars (02, 04, 05 and 07 in Table 1), whilst the other two, identified as H II regions, are in fact late-O main sequence stars (08 and 12 in Table 1).

Star 08 is the only object we have in common with the work by Gull et al. (2022, their star K1/B1), who classified all of their stars as main-sequence (class V) objects. Our O9 V classification matches the one provided by these authors. We note that, like these authors, we selected the brightest blue stars as candidates for the stellar spectroscopy. However, the brightest star observed by Gull et al. (2022), has a  $B$  magnitude of 20.1 (in the photometric catalogue of Stonkutė et al. 2014), while our sample includes, in addition to the object in common mentioned above, seven blue ( $B - V$  around  $-0.2$  to  $0.1$ ) stars brighter than this limit.

The outcome of our stellar classification procedure is reported in Column (7) of Table 1, and a few notes are presented below:

1. star 02: the emission at  $H\beta$  appears to be stellar since no extended nebular emission is detected at the wavelength of the Balmer lines and of  $[O II] \lambda 3727$ . This is the brightest object in our sample. We assign an Iab luminosity class because, although  $W_\gamma$  is consistent with the Ia class, the  $H\gamma$  line is likely partially filled with emission.
  2. in some cases  $W_\gamma$  is considerably larger than what the Azzopardi (1987) calibration yields for the Ib luminosity class, but is intermediate between classes Ib and III in Balona & Crampton (1974). For these objects, we assigned the luminosity class II (01, 03, 10). For star 09 the  $W_\gamma$  value we observe is consistent with class III in Balona & Crampton (1974). However, if we make a comparison with the absolute magnitudes of Galactic stars of the same spectral types we encounter a large discrepancy for the three A stars. The mean absolute magnitudes of A0 stars, calibrated with Hipparcos parallaxes by Wegner (2007), are  $M_V = -1.46$  (A0 II) and  $M_V = -0.09$  (A0 III), i.e. much fainter than observed for our targets (between approximately  $-2.9$  and  $-4.7$ ). Only with a luminosity classification of Ib we would find a correspondence with the Galactic stars. In the case of the B5 II star in our sample (01) there is no such issue: we measure  $M_V \simeq -3.0$ , while for this classification Wegner (2006) gives  $M_V = -2.82$ .
- This result could be hinting at the inadequacy of the method used here to estimate the luminosity class of our extremely metal-poor targets, at least of the A types. We have classified early-A stars as class II objects in other galaxies (e.g. WLM and IC 1613: Bresolin et al. 2006, 2007), but their absolute magnitudes are in line with the expectations from Galactic equivalents. On the other hand, as explained in Sec. 3, star 03 is found to be peculiar compared to the other stars, with a significantly fainter bolometric magnitude compared to the remaining stars.
3. star 08 is a O9 V star located inside H II region SHK 1 (Strobel et al. 1991). We are not aware of published spectra of this ionized nebula. This is star K1/B1 of Gull et al. (2022). Nebular contamination is clearly seen at  $H\beta$ , as shown by the spectrum in Fig. 2, while the two-dimensional spectra also show weak extended emission at  $H\gamma$ .

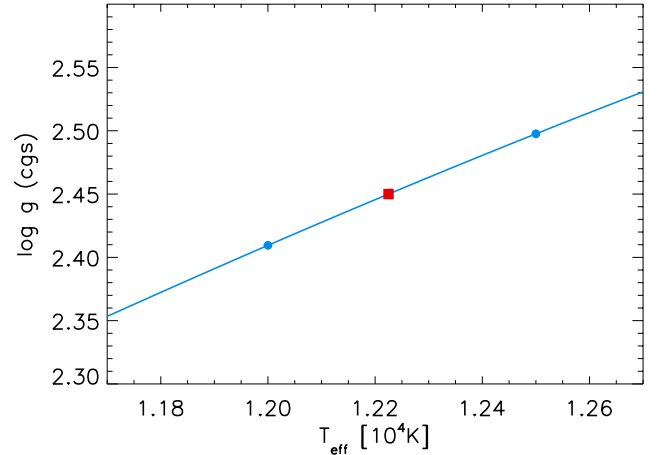
4. the O7/O8 V star 12 is the likely ionizing source of H II region SHK 4 (Strobel et al. 1991), which is region +112 – 020 of van Zee et al. (2006). The classification is made somewhat uncertain by the fact that the He I lines, used to estimate the spectral type, are filled in by emission, with  $\lambda 4713$  in emission and  $\lambda 4921$  completely filled in. We do not detect these lines in emission in the two-dimensional spectrum. Even He II  $\lambda 4686$  could be partially filled in. The fact that the [O III]  $\lambda\lambda 4959, 5007$  lines are easily seen in the two-dimensional spectrum is consistent with a higher ionization degree of SHK 4 compared with SHK 1, where such lines remain undetected. This is indirect evidence that star 12 is of an earlier spectral subtype than star 08.

### 3. QUANTITATIVE ANALYSIS

The goal of the quantitative spectral analysis is to determine the stellar atmospheric parameters effective temperature  $T_{eff}$ , surface gravity  $\log g$  and, most importantly, metallicity  $[Z]$  (defined as  $[Z] = \log Z/Z_{\odot}$ , where  $Z_{\odot}$  is number fraction of solar metallicity). Following the spectral classification we focus on the supergiants of spectral type late B and A and luminosity class Ib and II. Contrary to the O and early-B stars in our sample these objects have a relatively rich spectrum of metal lines and will allow for a reasonable metallicity determination even at the low metallicity of Leo A. Moreover, because of their relative brightness, the spectra have a high signal-to-noise ratio. This leaves us with seven objects for the quantitative analysis.

The analysis technique has been described in detail in previous papers (Kudritzki et al. 2014, 2016, Hosek et al. 2014, Bresolin et al. 2022). We compare the normalized observed spectra with synthetic spectra from a comprehensive grid of metal line-blanketed model atmospheres with extensive non-LTE line formation calculations using elaborate atomic models (Przybilla et al. 2006). The model grid described in Kudritzki et al. (2008, 2012) is adopted, comprising effective temperatures from 7900 K to 15000 K and gravities between 0.8 to 3.0 dex in cgs units (the exact upper and lower limits depend on  $T_{eff}$ , see Figure 1 in Kudritzki et al. 2008). The metallicity  $[Z]$  of the original grid ranges from  $-1.30$  dex to  $+0.50$  dex, however, because of the low metallicity of Leo A we have extended the grid to  $[Z] = -1.45$  dex.

In a first step, we use the observed Balmer lines ( $H_4$  to  $H_{10}$ ) to constrain  $\log g$  as a function of  $T_{eff}$  by finding the gravity at each fixed value of  $T_{eff}$  that fits the Balmer lines best. Figure 3 gives an example for target 04 of Table 1. The accuracy of the fit at each  $T_{eff}$  is 0.05 dex.



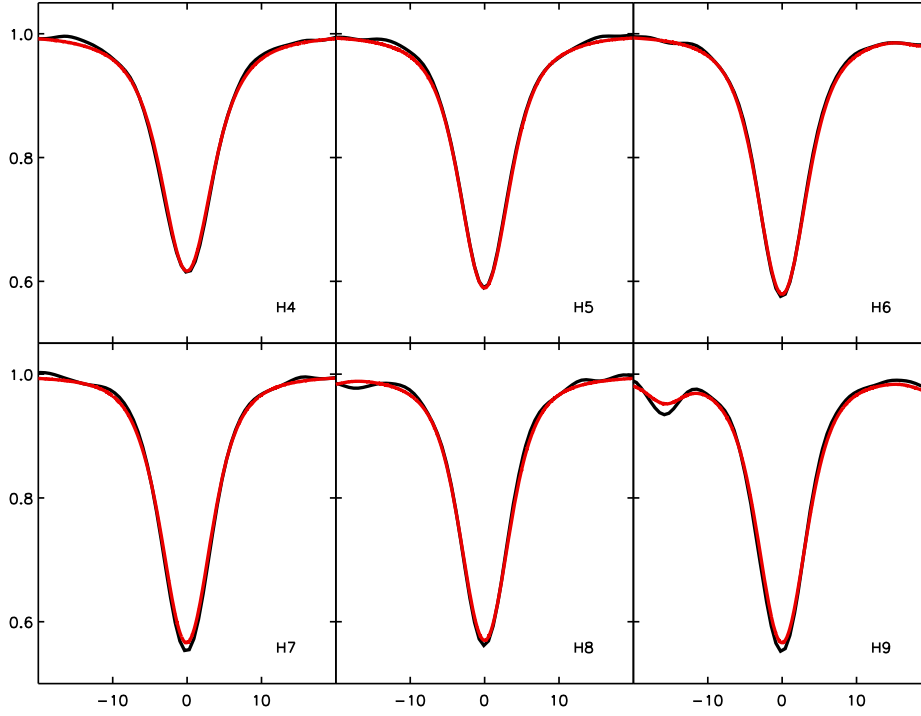
**Figure 3.** Balmer line fit of target 04 of Table 1. The blue curve shows the gravity  $\log g$  at which the best fit of the Balmer lines is obtained for each value  $T_{eff}$  on the abscissa. The red square shows the final  $\log g$  and  $T_{eff}$  values following from the additional fit of the metal lines along this curve (see text). The final  $\log g$  and  $T_{eff}$  for all targets analysed are given in Table 4.

Figure 4 shows the fit of the Balmer line profiles for the same target 04. The quality of the fit is excellent and is typical of what we obtain for all the remaining targets, for which the fits are not shown.

Subsequently, we move along the gravity-temperature relationship defined by the fit of the Balmer lines and compare observed and calculated fluxes as a function of metallicity in metal-line dominated spectral windows located away from the Balmer lines. We calculate  $\chi^2$  values at each  $T_{eff}$  and  $[Z]$ . We determine the minimum of  $\chi^2$  and isocontours in  $\Delta\chi^2$  around the minimum, which provides us with the determination of  $T_{eff}$  and  $[Z]$  and their uncertainties. From detailed Monte Carlo simulations (Hosek et al. 2014; Kudritzki et al. 2013) we know that the  $\Delta\chi^2 = 3$  and 9 isocontours provide a conservative estimate of the 1- and 2- $\sigma$  uncertainties, respectively (the minimum  $\chi^2$  values are of the order of unity). Figure 5 displays examples for three of the targets and Figures 6-7 show typical metal line fits.

We note from Figure 5 that some of our targets have stellar parameters which place them at the edges of our model grid. While its best fit occurs for  $T_{eff} = 8050$  K, target 10 could have a temperature below 7900 K, which is the lower temperature limit of our grid. In this case, the metallicity would be smaller than  $[Z] = -1.40$ . This is the only star at the temperature edge of our grid.

Targets 10 and 11 in Figures 6-7 have metallicities at the lower edge of our grid but the shape of the iso-



**Figure 4.** Balmer line fit of target 04 using the adopted  $T_{eff}$ ,  $\log g$ , and  $[Z]$  values in Table 2. Comparison of model (red) and observed (black) Balmer line profiles. The abscissa is the displacement from the line center in  $\text{\AA}$ .

**Table 2.** Stellar parameters.

| ID  | $T_{eff}$<br>(K)     | $\log g$<br>(cgs) | $[Z]$<br>(dex)          | $\log g_r$<br>(cgs)    | $E(B - V)$<br>(mag)    | $m_{bol}$<br>(mag) |
|-----|----------------------|-------------------|-------------------------|------------------------|------------------------|--------------------|
| (1) | (2)                  | (3)               | (4)                     | (5)                    | (6)                    | (7)                |
| 03  | $8450 \pm 200$       | $1.81 \pm 0.05$   | $-1.33 \pm 0.10$        | $2.11 \pm 0.15$        | $0.01^{+0.03}_{-0.01}$ | $21.09 \pm 0.11$   |
| 04  | $12225 \pm 250$      | $2.45 \pm 0.05$   | $-1.34 \pm 0.12$        | $2.10 \pm 0.06$        | $0.03 \pm 0.03$        | $18.78 \pm 0.12$   |
| 05  | $11850 \pm 200$      | $2.63 \pm 0.05$   | $-1.28 \pm 0.12$        | $2.34 \pm 0.06$        | $0.03 \pm 0.03$        | $19.47 \pm 0.11$   |
| 06  | $12725 \pm 250$      | $2.54 \pm 0.05$   | $-1.45 \pm 0.17$        | $2.12 \pm 0.06$        | $0.03 \pm 0.03$        | $18.87 \pm 0.12$   |
| 07  | $12275 \pm 200$      | $2.24 \pm 0.05$   | $-1.45 \pm 0.13$        | $1.88 \pm 0.05$        | $0.03 \pm 0.03$        | $18.46 \pm 0.11$   |
| 10  | $8050^{+150}_{-250}$ | $1.80 \pm 0.05$   | $-1.25^{+0.10}_{-0.25}$ | $2.18^{+0.25}_{-0.15}$ | $0.10 \pm 0.03$        | $19.40 \pm 0.11$   |
| 11  | $11650 \pm 200$      | $2.58 \pm 0.05$   | $-1.35 \pm 0.12$        | $2.32 \pm 0.06$        | $0.06 \pm 0.03$        | $19.16 \pm 0.11$   |

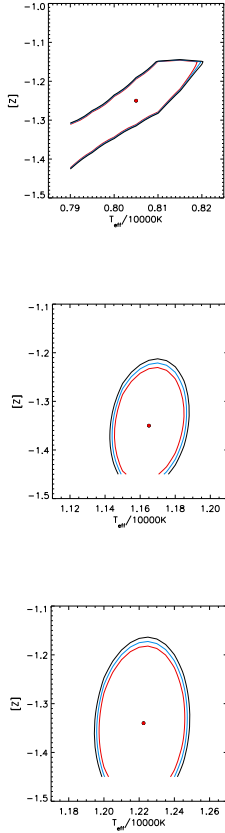
NOTE—The  $\log g$  uncertainty is for a fixed  $T_{eff}$  value.

contours allows an estimate of the uncertainty towards lower  $[Z]$  values. We encounter a similar situation for targets 06 and 07, whereas targets 03 and 05 have 1- $\sigma$  isocontours located fully inside the grid plane.

The spectroscopic parameters of the seven targets analyzed are given in Table 2. All have very low metallicities, with values between  $[Z] = -1.25$  and  $-1.45$ . The average metallicity value is  $[Z] = -1.35 \pm 0.08$ . We will discuss this result below in relation to all the other star-forming galaxies studied so far in our project. We note that our average stellar metallicity is in close agreement

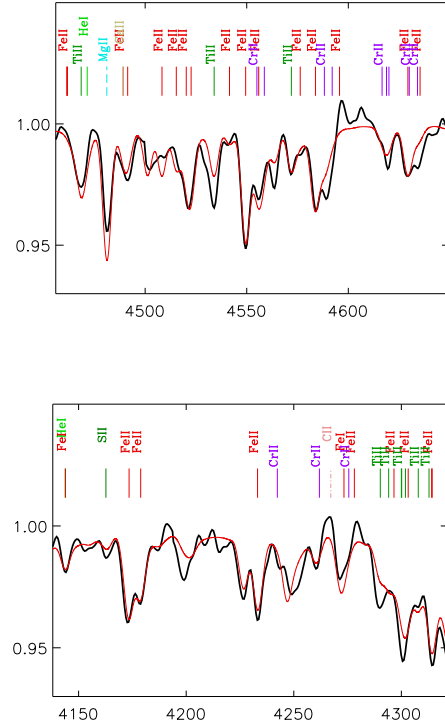
with results from the analysis of H II region emission lines:  $[Z] = -1.31 \pm 0.1$  (van Zee et al. 2006, semi-empirical method) and  $[Z] = -1.3 \pm 0.2$  (Ruiz-Escobedo et al. 2018, combination of direct method and photoionization modelling). The direct oxygen abundance based on the detection of the [O III]  $\lambda 4363$  line in a single H II region yields  $[Z] = -1.30 \pm 0.10$  (Ruiz-Escobedo et al. 2018).

Table 2 also contains the values of the flux-weighted gravity  $\log g_r = \log g - 4 \log(T_{eff}/10^4 \text{ K})$  of each target. As found by Kudritzki et al. (2003),  $\log g_r$  can



**Figure 5.** Determination of temperature and metallicity from  $\Delta\chi^2$  isocontours obtained through the comparison of observed and synthetic spectra (see text). Plotted are  $\Delta\chi^2 = 3$  (red), 6 (blue), and 9 (black) and the final fit values (red dot). The red and the black isocontours correspond to the 1- and 2- $\sigma$  uncertainties, respectively. (Top): target 10. (Middle) target 11. (Bottom): target 04.

be used to determine accurate spectroscopic distances through the flux-weighted gravity–luminosity relationship (FGLR) and we will apply this technique in Sect. 5. In addition, the value of  $\log g_F$  allows an assessment of evolutionary status and stellar masses through the spectroscopic Hertzsprung–Russel diagram (sHRD, see Langer & Kudritzki 2014), which is distance independent. Figure 8 presents this diagram for our Leo A BSG targets, together with MESA stellar evolution tracks calculated for  $[Z] = -1.25$  (Choi et al. 2016; Dotter 2016). We infer masses for our target stars in the range 7 to 12  $M_\odot$  (we note that  $[Z] = -1.25$  is somewhat higher than our average metallicity value, but using the next lower value  $-1.50$  in the MESA grid leads to very similar tracks and the same masses). These masses are lower than those in the range 15–40  $M_\odot$  found in our blue supergiant work in other galaxies (see Kudritzki et al.



**Figure 6.** Target 10: observed metal lines (black) and fit with the synthetic spectrum calculated for the final stellar parameters (red) in selected parts of the spectrum.

2016, Bresolin et al. 2022 and references therein) and the  $\log g_F$  values are correspondingly larger. This proceeds from the combination of the low stellar mass of this dwarf galaxy and the shape of the stellar initial mass function, which makes the presence of more massive stars more unlikely.

We note that all our seven spectroscopic targets are located in a region of the sHRD where stellar evolution theory predicts blue loop excursions for stars climbing the red giant branch. This is a consequence of the masses of our targets and the low metallicity. At larger masses and higher metallicity ( $[Z] \geq -0.90$ ) the MESA tracks do not show blue loops in the temperature range between 8000 K and 13000 K of our observed objects. Using the evolutionary tracks and focusing on this temperature range to estimate the time spent in the first HRD crossing towards the red giant branch and in the blue loops we find that the latter is larger by a factor of 30 to 120. Thus, it is extremely likely that our objects are stars in the blue loop stage. Note, however, our remarks concerning target 03 at the end of this section.

All stars included in this section on the quantitative analysis, except object 10, are identified as blue loop stars by Lešćinskaitė et al. (2022) based on their posi-

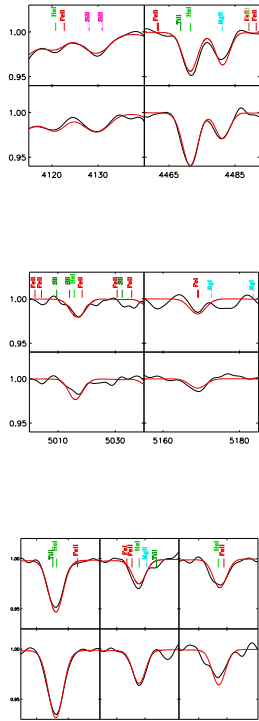


**Figure 7.** Targets 11 (at the top in each panel) and 04 (bottom): observed metal lines (black) and fit with the synthetic spectrum calculated for the final stellar parameters (red) in selected parts of the spectrum.

tion in color-magnitude diagrams. With the aid of stellar isochrones they derived ages between 30 Myr and 138 Myr for the targets we have in common.

Using the spectroscopic stellar parameters of  $T_{\text{eff}}$ ,  $\log g$ , and  $[Z]$  we calculate model spectral energy distributions (SEDs) and colors  $B - V$  and  $V - I$ . The comparison with the observed colors of Table 1 yields interstellar absorption color excesses  $E(B - V)$  and  $E(V - I)$ . With the relation  $E(B - V) = 0.75 E(V - I)$  (derived by applying the Cardelli et al. 1989 reddening law to the model SEDs) we obtain two  $E(B - V)$  values for each object and calculate the mean, which is given in Table 2. We then compute the interstellar extinction  $A_V = R_V \cdot E(B - V)$  with  $R_V = 3.3$  to correct the  $V$  magnitudes for reddening and apply the model atmosphere bolometric corrections to obtain apparent bolometric magnitudes  $m_{\text{bol}}$ . The latter are included in Table 2. We note that the amount of reddening is very small. This may be a selection effect because bright and blue objects were selected from the color magnitude diagrams for our spectroscopy.

Inspection of Table 2 immediately reveals that target 03 is more than two magnitudes fainter than all

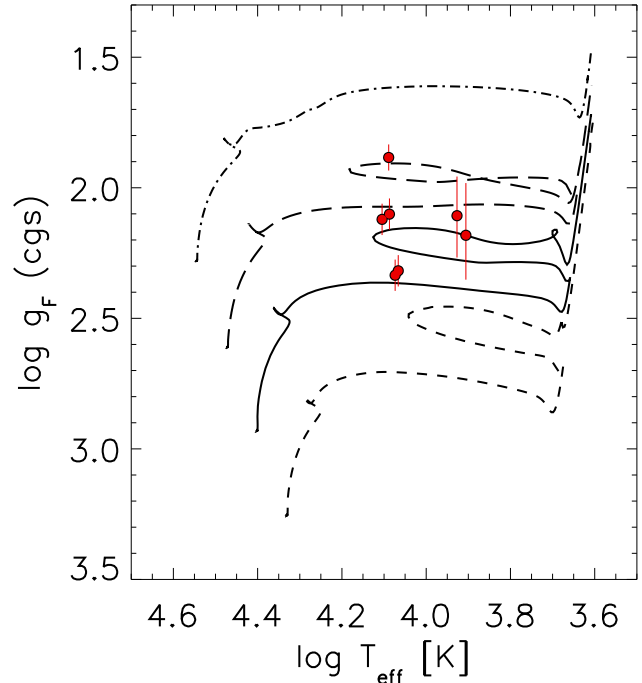


**Figure 8.** Spectroscopic Hertzsprung-Russell diagram of blue supergiant stars in Leo A together with MESA stellar evolution tracks calculated for  $[Z] = -1.25$  (Choi et al. 2016; Dotter 2016). The tracks include the effects of stellar rotation and are calculated for initial main-sequence masses of  $5 M_{\odot}$  (dashed),  $7 M_{\odot}$  (solid),  $10 M_{\odot}$  (long-dashed) and  $15 M_{\odot}$  (dashed-dotted).

the other targets of comparable  $\log g_F$ . It is by far the faintest object in our sample, while it should be among the brightest according to its flux-weighted gravity. We will discuss this target in detail in Sec. 6.

#### 4. LEO A AND THE MASS-METALLICITY RELATIONSHIP OF STAR-FORMING GALAXIES

With a stellar mass  $M_* = 3.3 \times 10^6 M_{\odot}$  (Leroy et al. 2019, corrected for the different galaxy distance adopted here) Leo A is the galaxy that has by far the lowest mass of the systems studied to date in our project (see Bresolin et al. 2022 for a summary). It is, thus, ideal to investigate how the tight relationship between stellar mass and stellar metallicity of the young stellar population (mass-metallicity relation, MZR) extends to very low galaxy stellar masses. Figure 9 shows how Leo A marks the end of a tight relationship stretching over four orders of magnitude in stellar mass. This confirms that the MZR can be nicely explained by simple galaxy evolution models that assume that galactic winds and matter infall result in a simple redshift-dependent relationship between galaxy gas mass and stellar mass (Kudritzki

et al. 2021). In this sense Leo A provides a crucial contribution towards the understanding of galaxy evolution.

In Figure 9 we have also added the results of the most recent study by Sextl et al. (2023). In this work spectra of 200000 SDSS star-forming galaxies stacked in bins of galaxy stellar mass were analysed using a population synthesis technique which allows to disentangle metallicity and ages of the young ( $\sim 0.2$  Gyr) and old ( $\sim 10$  Gyr) stellar population. The metallicities of the young population in the different galactic stellar mass bins are shown in Figure 9 as orange squares. They are in good agreement with metallicities obtained from the analysis of BSGs in nearby galaxies, confirming the concept of a universal mass-metallicity relationship in the low-redshift universe.

### 5. FLUX-WEIGHTED GRAVITY–LUMINOSITY RELATIONSHIP AND DISTANCE ESTIMATE

As found by Kudritzki et al. (2003, 2008) blue supergiant stars exhibit a correlation between bolometric magnitude and flux-weighted gravity, the flux-weighted gravity–luminosity relationship (FGLR), which can be used to determine accurate distances to galaxies. Figure 10 shows this relationship for the Leo A BSGs included in Table 2. The figure does not contain object 03 of Table 2 because it is a faint outlier as already discussed above.

We adopt the calibration of the FGLR by Urbaneja et al. (2017), obtained from the analysis of 90 BSGs, adjusted to the LMC distance modulus  $m - M = 18.477$  mag (Pietrzyński et al. 2019):

$$M_{bol} = 3.20(\log g_F - 1.5) - 7.878 \quad (1)$$

and determine a FGLR-based distance modulus of Leo A from a regression fit accounting for the errors in  $\log g_F$  and  $m_{bol}$ . We obtain  $m - M = 24.77 \pm 0.11$  mag. The green line in Figure 10 shows the fitting relation of Eq. (1), shifted by an amount equal to this distance modulus.

Our FGLR distance modulus is significantly larger than the value of  $24.40 \pm 0.06$  determined by Nagarajan et al. (2022) from RR Lyrae stars using a new Gaia eDR3-based calibration. While the ad hoc adoption of an RR Lyrae metallicity of  $[Z] = -2.0$  may add some additional uncertainty to this value, the distance modulus of the metal-poor dwarf galaxy IC 1613 that these authors report,  $m - M = 24.42 \pm 0.03$  mag, is in excellent agreement with the FGLR value of  $24.47 \pm 0.11$  mag (see Bresolin et al. 2022). This seems to rule out large systematic effects. On the other hand, we also note that Nagarajan et al. (2022) provide an average distance modulus literature value of  $24.48 \pm 0.12$  for Leo A, which

comes marginally close to the FGLR value, if the errors are considered. The Extragalactic Distance Database (Tully et al. 2009) gives a tip of the red giant branch (TRGB) distance modulus of  $24.35^{+0.47}_{-0.14}$  mag.

At face value the FGLR severely overestimates the distance to Leo A. However, there are a few important issues that must be considered to understand the reasons for the discrepancy. First of all, the sample of LMC BSGs used by Urbaneja et al. (2017) to obtain the calibration relationship of Eq. (1) consisted of objects of lower  $\log g_F$  and higher  $M_{bol}$ . No object in the LMC had a  $\log g_F$  value larger than 1.90. The application of Eq. (1) for the distance determination is, thus, an extrapolation of the calibration relationship. The uncertainty introduced by the extrapolation is very likely small. The BSGs in the low-metallicity dwarf galaxy WLM studied by Urbaneja et al. (2008) cover the usual range between 1.1 and 1.9 in  $\log g_F$ , but also include two objects with  $\log g_F = 2.2$  and  $\log g_F = 2.3$ . The fit with our present FGLR calibration to the WLM supergiants yields good agreement with the TRGB distance (see Sextl et al. 2021) and the two objects with high  $\log g_F$  agree with the extrapolated relationship.

More importantly, as discussed above all of the objects used for the FGLR distance fit are very likely objects in the blue loop stage. This means that their  $\log g_F$  values are about 0.2 dex lower than for BSGs in the same temperature range crossing the HRD for the first time towards the red giant stage. These blue loop objects are brighter than they were during their first crossing, but only by about 0.1 mag (see Figure 11). This implies that the FGLR of very low metallicity BSGs in the mass range we are considering and captured in the blue loop stage will be fainter than the FGLR of objects captured in their first crossing. This is shown in Figure 12, where we have connected the  $\log g_F$  and  $M_{bol}$  values of the MESA evolutionary tracks of Figures 8 and 11 in the  $T_{eff}$  range 7900-13000 K in order to construct the predicted FGLR for both first crossing and blue loop BSGs. We see that the differential shift of the blue loop FGLR amounts to  $\sim 0.25$  mag.

The third aspect in our Leo A FGLR discussion concerns the extremely low metallicity of the stars. The LMC BSG calibration sample of Urbaneja et al. (2017) had a metallicity of  $[Z] = -0.35$ . At the stellar luminosity and mass values of our Leo A targets there is an additional small metallicity effect, which impacts on both flux-weighted gravities and bolometric magnitudes. As Figure 12 illustrates, the FGLR of the first crossing at the higher metallicity of  $[Z] = -0.25$  (dark red curve) is 0.1 magnitudes brighter than at  $[Z] = -1.25$  (red curve). It is worth pointing out that Meynet et al. (2015) have al-

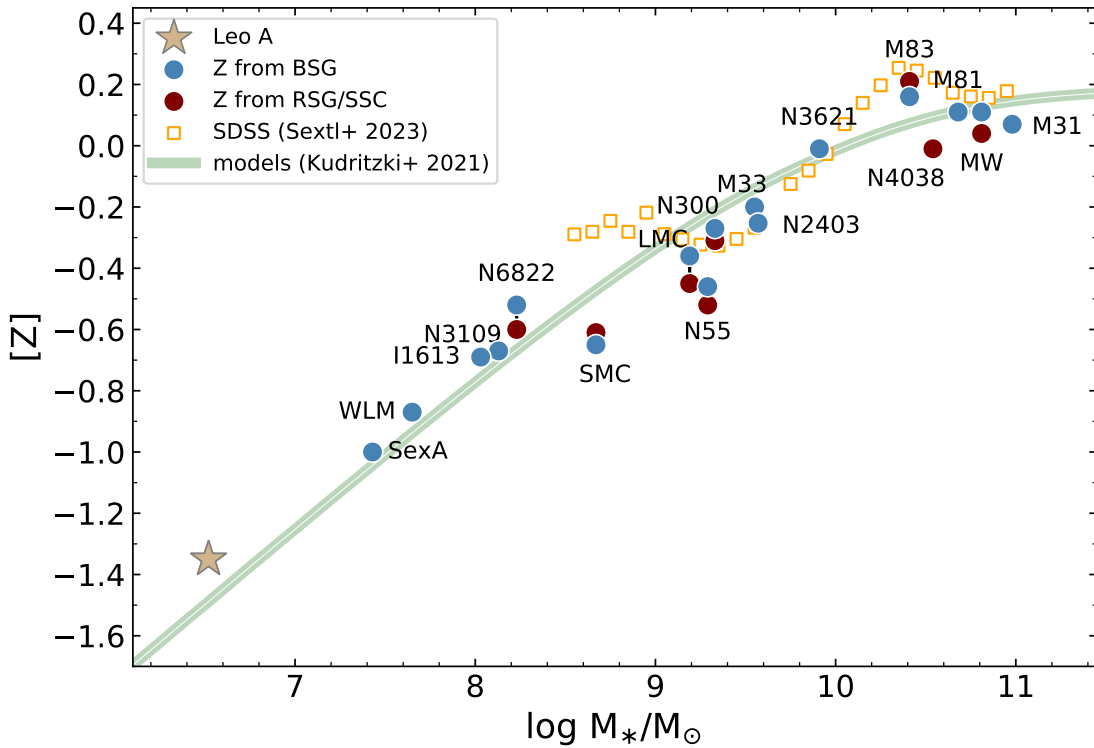


**Figure 9.** The mass-metallicity relationship of star-forming galaxies based on absorption line studies of the young stellar population. Results from blue supergiants (BSG) are shown in blue, while metallicities from red supergiants (RSG) and superstar clusters (SSC) are displayed in red. The yellow symbols correspond to the recent population synthesis study of 250,000 star-forming SDSS galaxies by Sextl et al. (2023). Our new result obtained for Leo A is represented with the star symbol. Predictions from the galaxy evolution look-back models by Kudritzki et al. (2021) are shown as the green curve.

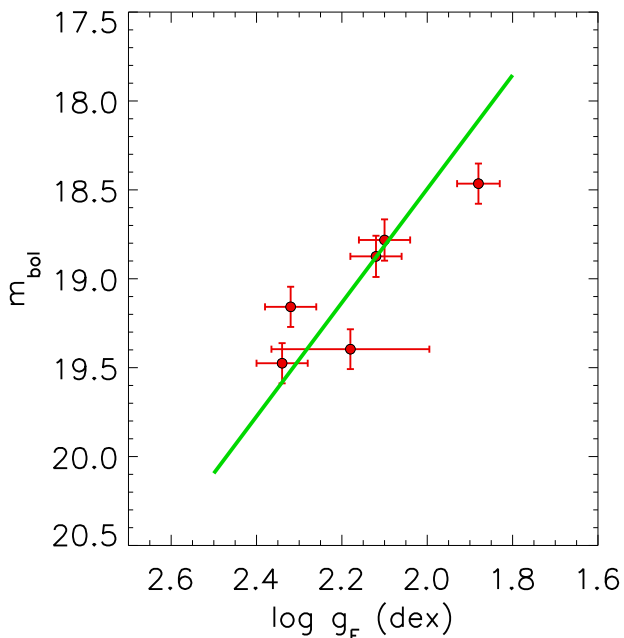


**Figure 10.** FGLR of Leo A blue supergiant stars. The green line is the fitting relation described in the text.

readily studied stellar evolution metallicity effects on the FGLR and found them to be small, but their work focused on higher stellar luminosities and did not consider the extremely low metallicities encountered in Leo A.

The combined differential effect of blue loops and extremely low metallicities amounts to a decrease of the bolometric magnitudes by 0.35 mag. The fact that we are using a FGLR calibration based on objects that are experiencing the first crossing of the HRD and approximately  $10\times$  the metallicities may explain why we obtain a distance modulus that is  $\sim 0.35$  mag larger than the one obtained by the careful RR Lyrae analysis of Nagarajan et al. (2022).

## 6. THE POST-AGB OBJECT 03

As we have already pointed out, object 03 of Table 2 is a faint outlier by at least 2 magnitudes in the FGLR. Assuming a distance modulus of 24.40 mag we obtain an absolute magnitude  $M_{bol} = -3.3$  mag for this star, corresponding to a luminosity  $\log L/L_{\odot} = 3.2 \pm 0.1$ , where the uncertainty comes from the  $m_{bol}$  error and a distance modulus error of 0.1 mag. This puts object 03 into the luminosity range of low-mass post-AGB objects, which have left the asymptotic giant branch

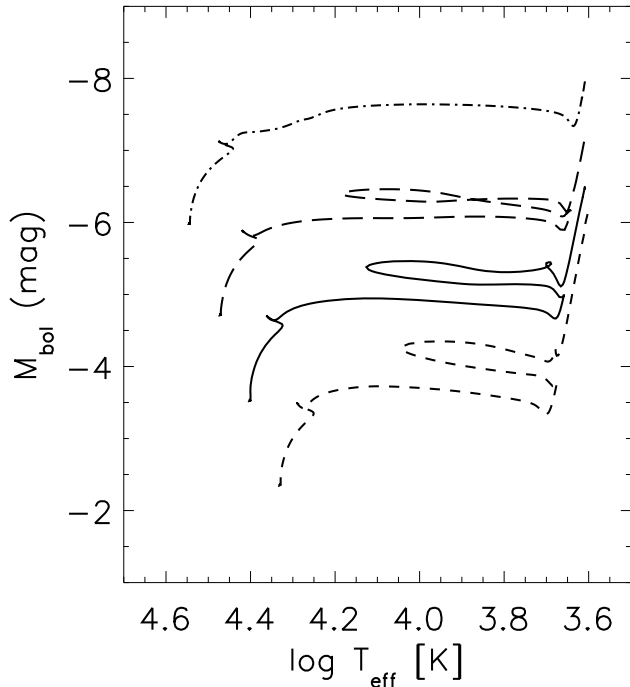


**Figure 11.** Hertzsprung-Russell diagram of MESA stellar evolution tracks calculated for  $[Z] = -1.25$  (Choi et al. 2016; Dotter 2016). The tracks include the effects of stellar rotation and are calculated for initial main-sequence masses of  $5 M_{\odot}$  (dashed),  $7 M_{\odot}$  (solid),  $10 M_{\odot}$  (long-dashed) and  $15 M_{\odot}$  (dashed-dotted).

and are on their way to becoming planetary nebulae. A typical low-metallicity post-AGB star with a mass of  $0.52 M_{\odot}$  would have a luminosity in this ballpark (see, for instance, Miller Bertolami 2016). Since  $\log g_f = \log M/M_{\odot} - \log L/L_{\odot} + 5.392$  (see Langer & Kudritzki 2014) we obtain  $\log g_f = 1.91 \pm 0.1$  dex for such an object, which agrees within the error margins with the flux-weighted gravity of object 03. We therefore conclude that target 03 is a low-mass post-AGB star.

As a low-mass post-AGB star object 03 is significantly older than the BSGs. Its age is very likely in the range of Gyrs. The fact that the metallicity we find,  $[Z] = -1.33 \pm 0.10$ , is similar to that of the BSGs confirms that the chemical enrichment in Leo A has been proceeding very slowly (Cole et al. 2007; Kirby et al. 2017). In this context we also point out that the metallicity of object 03 is very similar to that of the single planetary nebula known in Leo A (Skillman et al. 1989) and analyzed by van Zee et al. (2006), who obtained  $[Z] = -1.39 \pm 0.05$  (the re-analysis of the same data by Ruiz-Escobedo et al. 2018 gave  $[Z] = -1.35 \pm 0.02$ ).

## 7. SUMMARY

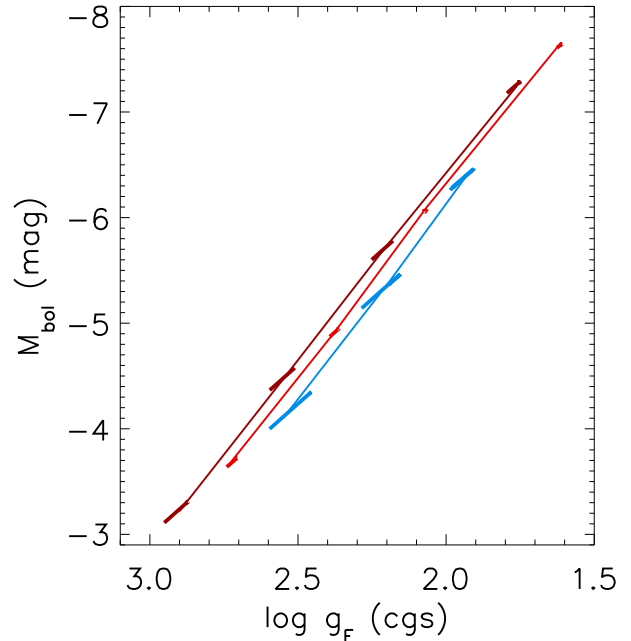


**Figure 12.** Stellar evolution FGLR at  $[Z] = -1.25$  constructed from Figures 8 and 11 for BSGs in the first crossing phase towards the red giant phase (red) and during the blue loop phase (blue). The FGLR plotted in dark red, also obtained from MESA evolutionary tracks, refers to the first crossing phase at  $[Z] = -0.25$ .

In this paper, we have presented new spectroscopic data for 12 among the visually brightest blue stars in the dwarf irregular galaxy Leo A and carried out the first quantitative analysis of blue supergiants in this galaxy. Within our series of studies on the quantitative spectroscopy of evolved massive stars in nearby star-forming galaxies, this look at Leo A is of special significance, given the known low gas-phase metallicity of this system, around 5% of the solar value.

The classification of the spectra shows that all our targets are individual stars in Leo A. The two located within the boundaries of known H II regions are late-O main-sequence stars and are likely powering the ionization of their respective host nebulae. The remaining objects are BA-type bright giants or supergiant stars, intrinsically less luminous than the majority of the stars we have investigated in other, more massive galaxies. We identify one of our targets as a post-AGB star, due to its significantly low bolometric luminosity for its value of the flux-weighted gravity, in comparison with the other stars that we have analyzed. The fact that the metallicity of this object is similar to that of the supergiant stars confirms that the chemical enrichment in Leo A is progressing very slowly.

We have measured the surface stellar parameters,  $T_{\text{eff}}$  and  $\log g$ , as well as the metallicity of seven stars, all of the spectral types between B8 and A0, by comparing the rectified observed spectra with a large grid of model spectra, despite the weakness of the metal lines which could hamper the heavy element analysis. We obtain remarkably similar values of the metallicity for the seven stars, with an average  $[Z] = -1.35 \pm 0.08$ , in superb agreement with the published gas-phase chemical abundance obtained from H II regions and one planetary nebula. This measurement allows us to place Leo A into the stellar mass–metallicity relation of star-forming galaxies derived from the spectroscopy of massive stars, rather than the emission-line analysis of the ionized gas, and which extends now over four orders of magnitude in mass, in nice agreement with theoretical predictions from simple galaxy evolution models.

From the stellar parameters and the flux-weighted–luminosity relation (FGLR) we derive a spectroscopic distance modulus  $m - M = 24.77 \pm 0.11$ . This result is significantly larger (by 0.37 mag) than the value indicated by RR Lyrae. This discrepancy is explained by the very low metallicity of Leo A, one order of magnitude below that of the FGLR calibrator (the LMC), and, most of all, by its effect on stellar evolution. In the  $T_{\text{eff}}$  interval that characterizes our targets, stellar evolution models calculated at a metallicity comparable to the one measured in Leo A show that: (i) the objects are very likely in the blue loop phase and (ii) the FGLR is affected by

the evolutionary stage of the stars as they evolve across the HRD. In fact, the relation is systematically fainter for stars that are observed while in the blue loop phase compared to those that are crossing the HRD for the first time towards the red giant phase. Such an effect is absent at the higher metallicities found in the other galaxies we have analyzed.

This research has made use of the Keck Observatory Archive (KOA), which is operated by the W. M. Keck Observatory and the NASA Exoplanet Science Institute (NExSci), under contract with the National Aeronautics and Space Administration. RPK acknowledges support by the Munich Excellence Cluster Origins funded by the Deutsche Forschungsgemeinschaft (DFG, German Research Foundation) under Germany’s Excellence Strategy EXC-2094 390783311. The authors wish to recognize and acknowledge the very significant cultural role and reverence that the summit of Maunakea has always had within the indigenous Hawaiian community. We are most fortunate to have the opportunity to conduct observations from this mountain.

*Facility:* Keck:I (LRIS)

*Software:* IRAF (Tody 1986, 1993), SciPy (Virtanen et al. 2020), NumPy (Harris et al. 2020), Matplotlib (Hunter 2007), PyRAF (Science Software Branch at STScI 2012).

## REFERENCES

- Adelman-McCarthy, J. K., Agüeros, M. A., Allam, S. S., et al. 2007, ApJS, 172, 634, doi: [10.1086/518864](https://doi.org/10.1086/518864)
- Asplund, M., Grevesse, N., Sauval, A. J., & Scott, P. 2009, ARA&A, 47, 481, doi: [10.1146/annurev.astro.46.060407.145222](https://doi.org/10.1146/annurev.astro.46.060407.145222)
- Azzopardi, M. 1987, A&AS, 69, 421
- Balona, L., & Crampton, D. 1974, MNRAS, 166, 203, doi: [10.1093/mnras/166.2.203](https://doi.org/10.1093/mnras/166.2.203)
- Bresolin, F., Kudritzki, R.-P., & Urbaneja, M. A. 2022, ApJ, 940, 32, doi: [10.3847/1538-4357/ac9584](https://doi.org/10.3847/1538-4357/ac9584)
- Bresolin, F., Kudritzki, R.-P., Urbaneja, M. A., et al. 2016, ApJ, 830, 64, doi: [10.3847/0004-637X/830/2/64](https://doi.org/10.3847/0004-637X/830/2/64)
- Bresolin, F., Pietrzyński, G., Urbaneja, M. A., et al. 2006, ApJ, 648, 1007, doi: [10.1086/506200](https://doi.org/10.1086/506200)
- Bresolin, F., Urbaneja, M. A., Gieren, W., Pietrzyński, G., & Kudritzki, R.-P. 2007, ApJ, 671, 2028, doi: [10.1086/522571](https://doi.org/10.1086/522571)
- Brown, W. R., Geller, M. J., Kenyon, S. J., & Kurtz, M. J. 2006, ApJ, 647, 303, doi: [10.1086/505165](https://doi.org/10.1086/505165)
- . 2007, ApJ, 666, 231, doi: [10.1086/519547](https://doi.org/10.1086/519547)
- Cardelli, J. A., Clayton, G. C., & Mathis, J. S. 1989, ApJ, 345, 245, doi: [10.1086/167900](https://doi.org/10.1086/167900)
- Choi, J., Dotter, A., Conroy, C., et al. 2016, ApJ, 823, 102, doi: [10.3847/0004-637X/823/2/102](https://doi.org/10.3847/0004-637X/823/2/102)
- Cole, A. A., Weisz, D. R., Dolphin, A. E., et al. 2014, ApJ, 795, 54, doi: [10.1088/0004-637X/795/1/54](https://doi.org/10.1088/0004-637X/795/1/54)
- Cole, A. A., Skillman, E. D., Tolstoy, E., et al. 2007, ApJL, 659, L17, doi: [10.1086/516711](https://doi.org/10.1086/516711)
- Dolphin, A. 2016, DOLPHOT: Stellar photometry, Astrophysics Source Code Library, record ascl:1608.013. <http://ascl.net/1608.013>
- Dolphin, A. E. 2000, PASP, 112, 1383, doi: [10.1086/316630](https://doi.org/10.1086/316630)
- Dotter, A. 2016, ApJS, 222, 8, doi: [10.3847/0067-0049/222/1/8](https://doi.org/10.3847/0067-0049/222/1/8)
- Evans, C. J., Bresolin, F., Urbaneja, M. A., et al. 2007, ApJ, 659, 1198, doi: [10.1086/511382](https://doi.org/10.1086/511382)
- Evans, C. J., & Howarth, I. D. 2003, MNRAS, 345, 1223, doi: [10.1046/j.1365-2966.2003.07038.x](https://doi.org/10.1046/j.1365-2966.2003.07038.x)

- Evans, C. J., Howarth, I. D., Irwin, M. J., Burnley, A. W., & Harries, T. J. 2004, *MNRAS*, 353, 601, doi: [10.1111/j.1365-2966.2004.08096.x](https://doi.org/10.1111/j.1365-2966.2004.08096.x)
- Fitzpatrick, E. L. 1991, *PASP*, 103, 1123, doi: [10.1086/132934](https://doi.org/10.1086/132934)
- Gallart, C., Monelli, M., Mayer, L., et al. 2015, *ApJL*, 811, L18, doi: [10.1088/2041-8205/811/2/L18](https://doi.org/10.1088/2041-8205/811/2/L18)
- Gull, M., Weisz, D. R., Senchyna, P., et al. 2022, *ApJ*, 941, 206, doi: [10.3847/1538-4357/aca295](https://doi.org/10.3847/1538-4357/aca295)
- Harris, C. R., Millman, K. J., van der Walt, S. J., et al. 2020, *Nature*, 585, 357, doi: [10.1038/s41586-020-2649-2](https://doi.org/10.1038/s41586-020-2649-2)
- Hosek, Jr., M. W., Kudritzki, R.-P., Bresolin, F., et al. 2014, *ApJ*, 785, 151, doi: [10.1088/0004-637X/785/2/151](https://doi.org/10.1088/0004-637X/785/2/151)
- Hunter, J. D. 2007, *Computing in Science & Engineering*, 9, 90, doi: [10.1109/MCSE.2007.55](https://doi.org/10.1109/MCSE.2007.55)
- Kirby, E. N., Cohen, J. G., Guhathakurta, P., et al. 2013, *ApJ*, 779, 102, doi: [10.1088/0004-637X/779/2/102](https://doi.org/10.1088/0004-637X/779/2/102)
- Kirby, E. N., Rizzi, L., Held, E. V., et al. 2017, *ApJ*, 834, 9, doi: [10.3847/1538-4357/834/1/9](https://doi.org/10.3847/1538-4357/834/1/9)
- Kudritzki, R. P., Bresolin, F., & Przybilla, N. 2003, *ApJL*, 582, L83, doi: [10.1086/367690](https://doi.org/10.1086/367690)
- Kudritzki, R. P., Castro, N., Urbaneja, M. A., et al. 2016, *ApJ*, 829, 70, doi: [10.3847/0004-637X/829/2/70](https://doi.org/10.3847/0004-637X/829/2/70)
- Kudritzki, R.-P., Teklu, A. F., Schulze, F., et al. 2021, *ApJ*, 910, 87, doi: [10.3847/1538-4357/abe40c](https://doi.org/10.3847/1538-4357/abe40c)
- Kudritzki, R.-P., Urbaneja, M. A., Bresolin, F., Hosek, Jr., M. W., & Przybilla, N. 2014, *ApJ*, 788, 56, doi: [10.1088/0004-637X/788/1/56](https://doi.org/10.1088/0004-637X/788/1/56)
- Kudritzki, R.-P., Urbaneja, M. A., Bresolin, F., et al. 2008, *ApJ*, 681, 269, doi: [10.1086/588647](https://doi.org/10.1086/588647)
- Kudritzki, R.-P., Urbaneja, M. A., Gazak, Z., et al. 2012, *ApJ*, 747, 15, doi: [10.1088/0004-637X/747/1/15](https://doi.org/10.1088/0004-637X/747/1/15)
- . 2013, *ApJL*, 779, L20, doi: [10.1088/2041-8205/779/2/L20](https://doi.org/10.1088/2041-8205/779/2/L20)
- Langer, N., & Kudritzki, R. P. 2014, *A&A*, 564, A52, doi: [10.1051/0004-6361/201423374](https://doi.org/10.1051/0004-6361/201423374)
- Lennon, D. J. 1997, *A&A*, 317, 871
- Leroy, A. K., Sandstrom, K. M., Lang, D., et al. 2019, *ApJS*, 244, 24, doi: [10.3847/1538-4365/ab3925](https://doi.org/10.3847/1538-4365/ab3925)
- Lešinskaitė, A., Stonkutė, R., & Vanevičius, V. 2022, *A&A*, 660, A79, doi: [10.1051/0004-6361/202142743](https://doi.org/10.1051/0004-6361/202142743)
- McConnachie, A. W. 2012, *AJ*, 144, 4, doi: [10.1088/0004-6256/144/1/4](https://doi.org/10.1088/0004-6256/144/1/4)
- Meynet, G., Kudritzki, R.-P., & Georgy, C. 2015, *A&A*, 581, A36, doi: [10.1051/0004-6361/201526035](https://doi.org/10.1051/0004-6361/201526035)
- Miller Bertolami, M. M. 2016, *A&A*, 588, A25, doi: [10.1051/0004-6361/201526577](https://doi.org/10.1051/0004-6361/201526577)
- Nagarajan, P., Weisz, D. R., & El-Badry, K. 2022, *ApJ*, 932, 19, doi: [10.3847/1538-4357/ac69e6](https://doi.org/10.3847/1538-4357/ac69e6)
- Oke, J. B., Cohen, J. G., Carr, M., et al. 1995, *PASP*, 107, 375, doi: [10.1086/133562](https://doi.org/10.1086/133562)
- Pietrzyński, G., Graczyk, D., Gallenne, A., et al. 2019, *Nature*, 567, 200, doi: [10.1038/s41586-019-0999-4](https://doi.org/10.1038/s41586-019-0999-4)
- Przybilla, N., Butler, K., Becker, S. R., & Kudritzki, R. P. 2006, *A&A*, 445, 1099, doi: [10.1051/0004-6361:20053832](https://doi.org/10.1051/0004-6361:20053832)
- Ruiz-Escobedo, F., Peña, M., Hernández-Martínez, L., & García-Rojas, J. 2018, *MNRAS*, 481, 396, doi: [10.1093/mnras/sty2265](https://doi.org/10.1093/mnras/sty2265)
- Science Software Branch at STScI. 2012, PyRAF: Python alternative for IRAF. <http://ascl.net/1207.011>
- Sextl, E., Kudritzki, R.-P., Weller, J., Urbaneja, M. A., & Weiss, A. 2021, *ApJ*, 914, 94, doi: [10.3847/1538-4357/abfafa](https://doi.org/10.3847/1538-4357/abfafa)
- Sextl, E., Kudritzki, R.-P., Zahid, H. J., & Ho, I. T. 2023, *ApJ*, 949, 60, doi: [10.3847/1538-4357/acc579](https://doi.org/10.3847/1538-4357/acc579)
- Skillman, E. D., Kennicutt, R. C., & Hodge, P. W. 1989, *ApJ*, 347, 875, doi: [10.1086/168178](https://doi.org/10.1086/168178)
- Stonkutė, R., Arimoto, N., Hasegawa, T., et al. 2014, *ApJS*, 214, 19, doi: [10.1088/0067-0049/214/2/19](https://doi.org/10.1088/0067-0049/214/2/19)
- Strobel, N. V., Hodge, P., & Kennicutt, Robert C., J. 1991, *ApJ*, 383, 148, doi: [10.1086/170771](https://doi.org/10.1086/170771)
- Tody, D. 1986, in *Society of Photo-Optical Instrumentation Engineers (SPIE) Conference Series*, Vol. 627, *Instrumentation in astronomy VI*, ed. D. L. Crawford, 733, doi: [10.1117/12.968154](https://doi.org/10.1117/12.968154)
- Tody, D. 1993, in *Astronomical Society of the Pacific Conference Series*, Vol. 52, *Astronomical Data Analysis Software and Systems II*, ed. R. J. Hanisch, R. J. V. Brissenden, & J. Barnes, 173
- Tully, R. B., Rizzi, L., Shaya, E. J., et al. 2009, *AJ*, 138, 323, doi: [10.1088/0004-6256/138/2/323](https://doi.org/10.1088/0004-6256/138/2/323)
- Urbaneja, M. A., Kudritzki, R.-P., Bresolin, F., et al. 2008, *ApJ*, 684, 118, doi: [10.1086/590334](https://doi.org/10.1086/590334)
- Urbaneja, M. A., Kudritzki, R.-P., Gieren, W., et al. 2017, *AJ*, 154, 102, doi: [10.3847/1538-3881/aa79a8](https://doi.org/10.3847/1538-3881/aa79a8)
- van Zee, L., Skillman, E. D., & Haynes, M. P. 2006, *ApJ*, 637, 269, doi: [10.1086/498298](https://doi.org/10.1086/498298)
- Virtanen, P., Gommers, R., Oliphant, T. E., et al. 2020, *Nature Methods*, 17, 261, doi: [10.1038/s41592-019-0686-2](https://doi.org/10.1038/s41592-019-0686-2)
- Walborn, N. R. 1971, *ApJS*, 23, 257, doi: [10.1086/190239](https://doi.org/10.1086/190239)
- Walborn, N. R., & Fitzpatrick, E. L. 1990, *PASP*, 102, 379, doi: [10.1086/132646](https://doi.org/10.1086/132646)
- Walborn, N. R., Lennon, D. J., Heap, S. R., et al. 2000, *PASP*, 112, 1243, doi: [10.1086/316617](https://doi.org/10.1086/316617)
- Wegner, W. 2006, *MNRAS*, 371, 185, doi: [10.1111/j.1365-2966.2006.10549.x](https://doi.org/10.1111/j.1365-2966.2006.10549.x)
- . 2007, *MNRAS*, 374, 1549, doi: [10.1111/j.1365-2966.2006.11265.x](https://doi.org/10.1111/j.1365-2966.2006.11265.x)